RESEARCH ARTICLE

Experimental investigation on the degradation of turbulent friction drag reduction over semi-circular riblets

Wenfeng Li[1] · Shenghong Peng[1] · Hengdong Xi[1] · Wolfgang Schröder[2]

Abstract

Experimental investigations of turbulent boundary-layer flows over a semi-circular riblet surface were conducted to study the mechanisms of friction drag reduction. Particle-image velocimetry (PIV) was performed to analyze the statistics of the turbulent boundary layer and the structural properties of the large-scale motions and hotwire anemometry (HWA) was conducted to determine the energy spectra of the near-wall turbulent structures. The skin friction coefficients varied from drag reduction of -5.75% via 0.3% to 10.7% drag increase for riblet spacings in inner units of 17, 31.3, and 50.4 at three freestream velocities. The analyses of the near-wall flow structures indicate that the streamwise coherence is enhanced in the drag reduction regime, while the spatial correlation of the near-wall turbulent flow structures is reduced in the drag neutral and increase regimes. The streamwise energy spectra indicate that in the near-wall region, the energy content is increased by coherent structures at wavelength in inner units in the range of 100–300 for the drag increase regime.

1 Introduction

Drag reduction is one of the essential objectives in engineering science to satisfy the economical requirements and environmental constraints for transportation systems. In particular, friction drag contributes over 50 % to the total drag of large commercial airplanes (Schrauf et al. 2006) and up to 90% of marine vessels (Monty et al. 2016). This means friction drag reduction is one of the key factors to develop greener transportation systems. Hence, numerous passive and active flow control methods have been developed in the past decades including micro-structured surfaces (Choi 1989, Walsh 1983), super-hydrophobic materials (Daniello et al. 2009, Lee and Kim 2011), MEMS-based feedback control (Kasagi et al. 2009), open/closed-loop large-scale wall motions (Bai et al. 2014, Gatti et al. 2015, Gouder et al. 2013, Li et al. 2015, Wong et al. 2021) to mention just a few. Among them, the longitudinal micro-grooves, i.e., riblets, have been found to reduce friction drag by up to 10% in

laboratory experiments (Bechert et al. 1997) and a few percent in realistic flight conditions (Spalart and McLean 2011, Szodruch 1991). Riblets have been recognized as one of the most promising and efficient drag reduction techniques for engineering applications.

Systemic investigations on the drag reduction of riblets can be traced back to Walsh et al. (1982, 1983, 1984) who showed that different riblet geometries can reduce the friction drag by up to 8% in turbulent boundary layers (TBLs). Subsequently, a considerable amount of experimental and numerical investigations were conducted to study the dependence of friction drag on the riblet geometry (Bechert et al. 1997, Endrikat et al. 2020), pressure gradient (Debisschop and Nieuwstadt 1996), Reynolds number (Raayai-Ardakani and McKinley 2017), and flow incidence (Tiainen et al. 2020). These investigations showed that the variation in viscous drag above riblets strongly depends on the riblet spacing $s^+ = s u_\tau / \nu$, which is defined in inner units, i.e., s is the peak-to-peak distance, u_τ is the friction velocity, and ν is the kinematic viscosity of the fluid. Depending on the interaction of the wall-bounded turbulence above riblet surfaces, the friction drag variation can be divided into three s^+ regimes, i.e., the viscous regime, the viscous breakdown regime, and the drag increase regime or the so-called roughness regime (Garcia-Mayoral and Jiménez 2011).

In the viscous regime, the drag reduction ratio is proportional to the riblet spacing for $s^+ \leq 8$ due to the negligible

✉ Wenfeng Li
w.li@nwpu.edu.cn

1 School of Aeronautics and Institute of Extreme Mechanics, Northwestern Polytechnical University, Xi'an, Shannxi SN 29, People's Republic of China

2 Institute of Aerodynamics, RWTH Aachen University, Aachen, Germany

contribution of the nonlinear interaction of the riblets to the near-wall flow. The drag reduction mechanism in this regime has been fairly well described by Bechert and Bartenwerfer (1989) and Luchini et al. (1991) by the concept of protrusion height that quantifies the relation between riblet geometry and the amount of friction reduction. The viscous regime breaks down at $s^+ \approx 10$ due to the nonlinear interaction of the near-wall flow with riblets and leads to the maximum drag reduction for $s^+ \approx 15 - 20$. Garcia-Mayoral and Jiménez (2011) suggested that the optimum performance of riblets, regardless of the riblet shape, is obtained at $l_g^+ = l_g u_\tau / \nu \approx 11$ when l_g is defined by the square root of the groove cross section area $l_g = \sqrt{A_g}$.

Beyond the viscous regime, the saturation of drag reduction is not fully understood due to the complex interaction of the near-wall turbulence above the riblets structures. Several mechanisms have been proposed based on the nature of the flow, i.e., the structural behavior and statistical properties of wall-bounded turbulence. One mechanism is related to the relocation of the quasi-streamwise vortices (QSVs) which has been experimentally investigated by Lee and Lee (2001) using flow visualization in a low-speed wind tunnel and by Martin and Bhushan (2014) using large-eddy simulations (LESs). At small riblet spacing , i.e., $s^+ < 15$, QSVs with a typical diameter of roughly 30 wall units occur only above the riblet contour such that they can only interact with the protruding tips and result in blocking momentum transfer. When the riblet spacing becomes larger than $20 - 30$ viscous units, QSVs occur inside the riblets grooves and cause early drag degradation by transporting additional momentum toward the wall (Goldstein and Tuan 1998). For wider spaced riblets, a large area of riblet surface is exposed to the downwash of the high-speed flow induced by the QSVs. Ultimately, the friction drag surpasses the smooth wall drag and the drag increases at $s^+ \geq 30 - 40$.

Another interpretation on the drag degradation in the viscous breakdown regime was attributed to the appearance of large-scale spanwise roller structures that are triggered by Kelvin-Helmholtz (K-H) instability. Garcia-Mayoral and Jiménez (2011) stated that the K-H instability triggers the onset of spanwise rollers with a typical streamwise wavelength in inner coordinates of $\lambda^+ = 150$ in the flow field 20 wall units immediately above blade-shaped riblets with spacing beyond the optimal size in channel flows. In addition, they suggested that the K-H rollers were associated with extra Reynolds stresses that account for drag degradation of the blade-shaped riblets. More recently, Endrikat et al. (2020, 2021) carried out extensive direct numerical simulation (DNS) using a minimal-span channel approach for several riblet shapes with spacing from the drag reduction to drag increase regimes. They pointed out that the onset of the spanwise roller depends on the geometries of riblets and reported that the K-H rollers only exist for large

sharp-triangular and blade-shaped riblets. However, they do not occur for blunt-triangular and trapezoidal riblets. Based on the same DNS database, Modesti et al. (2021) reported that dispersive stresses carried by secondary flows can contribute significantly to the drag degradation of riblets.

The concise literature review has shown that riblets vary the friction drag by influencing the interaction of the turbulent structures in the near-wall region. We find that most studies are limited to internal flows, e.g., fully developed channel flow, whereas flows over transportation systems are external flows, i.e., turbulent boundary layer flow dominates skin friction drag. Moreover, a few fundamental aspects as to drag degradation are still to be investigated although extensive numerical and experimental analyses have been performed. To cover this gap, we conducted measurements on the statistical and structural characteristics of zero-pressure gradient (ZPG) turbulent boundary layers (TBLs) at several Reynolds numbers over riblets in several drag variation regimes, i.e., the drag reduction (DR) regime with a reduced friction drag, the drag neutral (DN) regime with no friction drag variation, and the drag increase (DI) regime with an increased friction drag. To analyze the turbulent statistics and the large-scale structures, a large-scale 2D-2C particle-image velocimetry (PIV) system with six cameras was used to capture the instantaneous velocity field in the streamwise (x) and wall-normal (y) plane. Additionally, hotwire anemometry measurements were performed above the riblets to determine the nature of turbulent spectra. The turbulent statistics, the near-wall flow structures, and the energy spectra for various drag variation regimes are analyzed to reveal the drag degradation mechanism of riblets.

This manuscript is organized as follows. In Sect. 2, we present the details of the measurement techniques and the data post-processing methods. In Sect. 3, we discuss the present results including the turbulence statistics, the structural characteristics, and the streamwise energy spectra at the DR, DN, and DI regimes. Finally, conclusions are given in Sect. 4.

2 Experimental setup, measurement, and post-processing methods

2.1 Flow facility and riblet surface

The measurements were conducted in a subsonic Göttingen-type wind tunnel with an open test section of 1800 mm long and a cross-sectional area of 1200×1200 mm^2 as shown in Fig 1a. The turbulent intensity based on the root-mean-square (RMS) of the streamwise velocity fluctuation is less than 0.3% of the freestream velocity U_∞. In the test section, a flat plate being 1750 mm long, 1200 mm wide, and 20 mm thick is horizontally installed in the test section to generate a
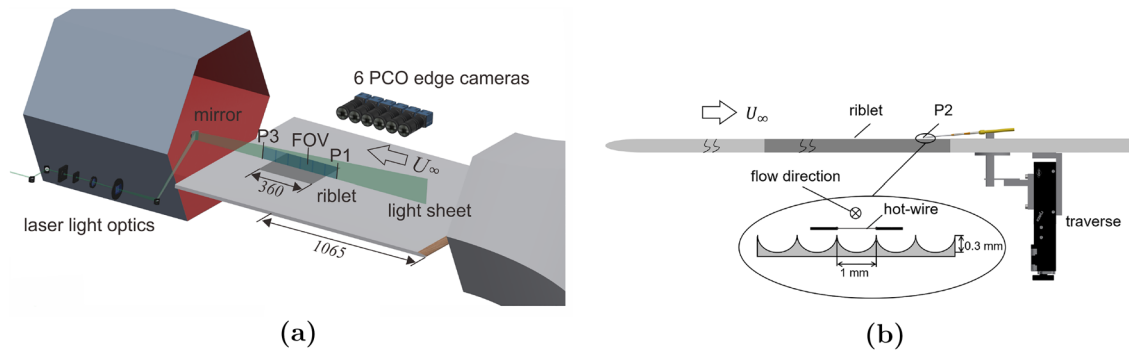
Fig. 1 Illustration of the experimental setup, **a** the arrangement of the flat plate and the 6-camera PIV system, **b** the riblet surface and the hotwire mount installed from the bottom of the flat plate

ZPG boundary layer. The origin $x = 0$ mm is defined at the leading edge. A tripping wire with a diameter of 0.5 mm located at $x = 60$ mm downstream of the 1:6 elliptical leading edge triggers flow transition such that a turbulent boundary layer is fully developed downstream of $x = 1020$ mm. At the center of the flat plate, the smooth wall can be replaced by a riblet surface insert starting from $x = 1065$ mm. The insert extends 360 mm in the streamwise direction and 180 mm in the spanwise direction. The PIV measurements were conducted between P_1 at $x_1 = 1020$ mm and P_3 at $x_3 = 1490$ mm, i.e., P_1 and P_3 denote the starting and ending points of the PIV field of view (FOV), and the hotwire measurements were located at P_2 at $x_2 = 1400$ mm.

As listed in Table 1, the experiments were conducted at three freestream velocities, i.e., $U_\infty = 5.95$, 11.79, and 19.74 m/s. The Reynolds numbers $Re_\theta = \theta U_\infty / \nu$ based on the momentum thickness θ and the freestream velocity U_∞ vary from 1217 to 1719, 1964 to 2814, and 3071 to 4092 for the smooth wall TBLs between P_1 and P_3.

The riblet structure shown in Fig. 1b was produced by the Institute of Metal Forming of the RWTH Aachen University via a rolling process (Hirt and Thome 2008). The riblet structure possesses a semi-circular geometry with a spanwise peak-to-peak spacing of $s = 1$ mm and a tip to valley height of $h = 0.3$ mm. Considering the nearly constant friction

velocity with variation smaller than 5% in the streamwise direction along with the insert (listed in Table 1), the riblet spacing in viscous unit is normalized based on the friction velocity at P_2 for simplification. Hence, the inner-scaled riblet spacings $s^+ = s u_\tau / \nu$ are 17.0, 31.7, and 50.4 for the three freestream velocities based on the friction velocity at P_2.

2.2 Multi-camera particle-image velocimetry

To capture the flow fields of the spatially developing TBLs, a six-camera 2D-2C PIV system sketched in Fig. 1a was used to achieve a high spatial resolution for the measurement field of view (FOV) with a streamwise to wall-normal aspect ratio of 8. The PIV system consists of a Spitlight 600 single cavity Nd:YAG laser with a maximum output pulse energy of 400 mj, six PCO Edge 5.5 double-frame cameras with a resolution of 2560×2160 pixels, and six Tamron lenses with a focal length of 180 mm and a maximum aperture of F3.5. The cameras were aligned with a slightly overlapping FOV between the adjacent FOVs along the streamwise direction such that the small FOVs can be sampled into a large FOV in the data post-processing.

Di-2-Ethyl-Hexyl-Sebacat (DEHS) tracer particles with a mean diameter of approximately 1 μm were injected into the freestream via a pipe fixed in the wind tunnel diffuser, which

Table 1 Experimental parameters of the turbulent boundary layers at several freestream velocities between the measurement points P_1 and P_3. The notations DR, DN, and DI denote drag reduction, drag neutral, and drag increase. The riblet spacing s and the height h are normalized based on the friction velocity $u_{\tau,0}$ of the smooth wall at P_2 since the friction velocity in the streamwise direction is nearly constant

$U_\infty (ms^{-1})$	Type	Re_θ	$u_\tau (ms^{-1})$	δ(mm)	s^+	h^+
5.95	Smooth	1217–1718	0.261–0.252	27.9–36.5	–	–
	Riblet (DR)	1182–1660	0.259–0.253	28.3–36.3	17.0	5.1
11.78	Smooth	1964–2814	0.480–0.475	23.8–31.4	–	–
	Riblet (DN)	1994–2822	0.487–0.465	24.6–31.7	31.7	9.4
19.74	Smooth	3071–4092	0.775–0.771	22.3–28.5	–	–
	Riblet (DI)	3087–4150	0.776–0.734	23.0–28.7	50.4	15.1

led to a homogeneous particle distribution in the test section. A laser light sheet being roughly 0.5 mm thick and 80 mm wide was generated by a set of optics to illuminate the tracer particles. To minimize light saturation at the wall, the laser light sheet was adjusted perpendicular to the flat plate and parallel to the freestream direction via a reflective mirror installed at 500 mm downstream of the flat plate. As stated before, the measurement FOV in the streamwise direction is located from P_1 at $x_1 = 1020$ mm to P_3 at $x_3 = 1490$ mm, i.e., starts 45 mm upstream of the insert and ends 65 mm downstream of the trailing edge of the insert. For all PIV measurements, the sampling rate is 10 Hz. In total, 10,000 independent flow fields for each case were captured.

The PIV data from each camera were evaluated by a multi-grid algorithm based on the window cross-correlation algorithm by Soria Soria (1996). The correlation window size was initially set to 64×64 pixels and, finally, changed to 24×12 pixels. With an overlap of 50%, the vector spacing of 0.44×0.22 mm in the streamwise and the wall-normal direction was achieved for the final integration. A normalized median test filter (Westerweel and Scarano 2005) over 3×3 vectors detected the invalid vectors. For the instantaneous flow field, the cross-correlation results indicate more than 99% valid vectors. In Fig. 2, the instantaneous flow field is composed of six small flow fields. In total, the FOV consists of 1200×300 vectors and covers an area of 470 mm $\times$ 75 mm. Thus, the large-scale structures in the outer boundary layer and the fine small-scale structures near the wall are efficiently captured. According to Benedict and Gould (1996), a 95% confidence interval of a true value $\overline{m}$ is within the interval $\overline{m} \pm 1.96\sqrt{(var(\overline{m}))}$, where $var(\overline{m})$ is the variance of the measured value. For the streamwise velocity U and velocity fluctuations u'_{rms}, the variances are $\overline{u'^2}/N$ and $[\overline{u'^4} - (\overline{u'^2})^2]/(4N\overline{u'^2})$ with N the number of samples. The theoretical sampling errors of the mean velocity and velocity fluctuations u and u'_{rms} on a 95 % confidence interval are lower than 0.3 % and 1 % with 10,000 PIV snapshots.

2.3 Hotwire anemometry

The hotwire anemometry (HWA) measurements were performed using a single boundary layer type probe with an active length of $l = 1$ mm. The diameter of the wire is $d = 5$ μm corresponding to $l/d = 200$ such that the criterion of preventing the end-conducting effect is satisfied. An IFA 300 constant temperature anemometer (CTA) system from TSI in conjunction with a 12-bit A/D converter was used for the data acquisition. The hotwire measurements were performed in the constant temperature mode with an overheat ratio of 0.5. Furthermore, an offset of 1 volt and a gain ratio of 10 were applied to the CTA system such that the full measurement range of the A/D converter could be used. The data sampling rate was set to 50 kHz with a measurement

duration of 83 seconds for each measurement location to ensure converged turbulence statistics data. In addition, a high-pass filter with a cutoff frequency of 10 Hz filtered out the low-frequency noise. The hotwire was calibrated *in situ* through a Pitot tube located in the freestream and a quartic polynomial was used to determine the calibration function.

As sketched in Fig. 1b, a LIMES LTM 60-20 HSM motorized traverse positioned the hotwire probe in the wall-normal direction with an accuracy of ± 4 μm. The position range was from 0 to 20 mm, thus only the lower part of the TBLs was measured. At 50 measurement points distributed in the wall-normal direction from $y = 0.05 \sim 17$ mm, the boundary-layer flow was recorded. The initial measurement step was 400 μm at $y = 17$ mm, and it was decreased to 200 - 50 μm when the probe approached the wall. In the region $y < 200$ μm, the measurement step was further reduced to 10 μm.

Note that, the spanwise spatial resolution of the hotwire is related to the active l length of the wire (Ligrani and Bradshaw 1987). For an efficient acquisition of the small-scale structures in TBLs, $l^+ = lu_\tau/\nu$ needs to be less than 20 viscous units such that the smallest structures can be resolved. At the highest freestream velocity, the active length of the wire is 50.4 viscous units, which introduces an spanwise filtering effect on the small-scale structures. A comparable spatial filtering effect also exists in the PIV measurement due to the finite interrogation window as listed in Table 2. In this study, we analyze the characteristics of the large-scale structures and as such the measured flow feature will not be affected by the spatial filtering effect. Furthermore, the spatial attenuation due to the over-long wire and the finite PIV correlation window is nominally comparable for the smooth and the riblet cases at similar Reynolds numbers.

3 Results and discussion

The skin friction drag above the smooth and riblet surfaces is examined to determine the variation in the skin friction in Sect. 3.1. Subsequently, the mean velocity distributions, streamwise and wall-normal velocity fluctuations, and the Reynolds shear stress are studied in Sect. 3.2. Finally, the modifications on the flow structures by the riblets are

Table 2 Spatial resolutions of the PIV and hotwire measurements

$U_\infty (ms^{-1})$	Vector spacing $x \times y$ (mm)	Δx^+	Δy^+	l^+
5.95	0.44×0.22	7.48	3.74	17.0
11.78	0.44×0.22	13.76	6.88	31.3
19.74	0.44×0.22	22.19	11.09	50.4

Fig. 2 The instantaneous flow field measured by the six-camera PIV system at $U_\infty =$ 5.95 m/s
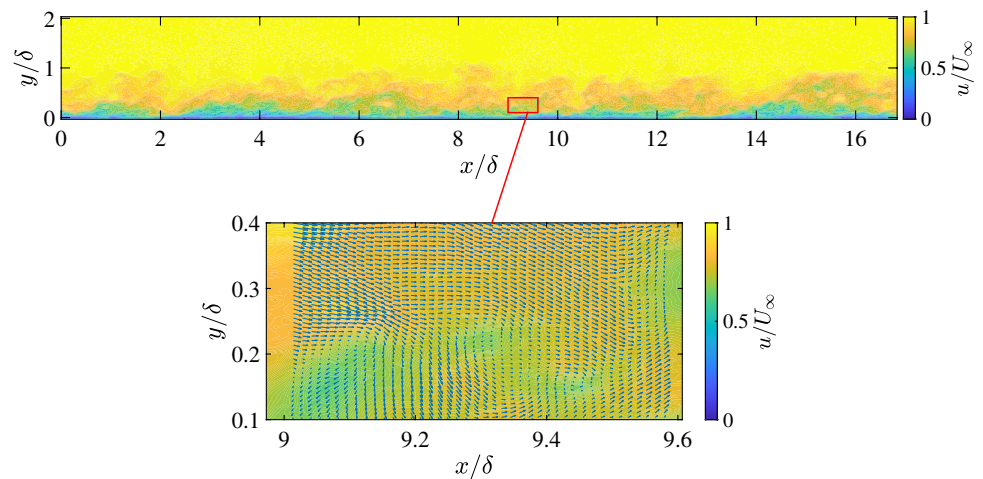
analyzed by comparing the two-point correlations, the large-scale structures, and the energy spectra in Sect. 3.3.

3.1 Skin friction drag

Based on the PIV and HWA data, the friction drag is determined from the streamwise velocity distributions above the smooth and riblet walls. A modified Clauser method (Nugroho et al. 2013, Perry and Li 1990, Xu et al. 2019) is implemented to obtain the friction velocity u_τ by fitting the streamwise velocity profiles to a modified log-law, which reads

$$\frac{U}{u_\tau} = \frac{1}{\kappa} ln \frac{u_\tau(y + \Delta y)}{\nu} + A - \frac{\Delta U}{u_\tau} \qquad (1)$$

where Δy is the wall-normal offset of the origin above the riblet surface, κ is the von Kármán constant, A is the log-law intercept of the smooth wall, and $\Delta U/u_\tau$ is the roughness function. By differentiating Eq. (1) with respect to y, the intercept of the log-law A and the roughness function $\Delta U/u_\tau$ can be eliminated and yields

$$u_\tau = \kappa(y + \Delta y)\frac{dU}{dy}. \qquad (2)$$

The friction velocity u_τ and the wall-normal offset of the origin Δy are determined by fitting the streamwise velocity profiles in the logarithmic region ($50 \le y^+ \le 130$) to Eq. (2) using a least squares method. The friction coefficient C_f is then determined by $C_f = 2u_\tau^2/U_\infty^2$. For all riblet cases, the wall-normal offset of the origin is roughly $0.8h$ with a variation of $\pm 0.05h$. This agrees with the wall-normal offset determined in Choi (1989) above rectangle riblets. It has been suggested that the wall-normal offset depends not only on the riblet geometry but also on the Reynolds number (Chung et al. 2021). However, an more accurate estimation

of Δy is not feasible due to the uncertainty of the PIV and HWA experiments.

The drag reduction ratio DR is defined by the variation in the friction coefficients, i.e., $DR = (C_{f,r}/C_{f,s} - 1) \times 100\%$, where $C_{f,s}$ and $C_{f,r}$ are the friction coefficients of the smooth and riblet walls. Hence, a negative DR indicates drag reduction while a positive DR shows drag increase. At the three freestream velocities $U_\infty = 5.95$, 11.78, and 19.74 m/s, the friction drag variations are -5.75%, 0.3%, and 10.7% above the riblet wall for $s^+ = 17.0$, 31.3, and 50.4, which indicates the drag reduction (DR), drag neutral (DN), and drag increase (DI) cases.

3.2 Turbulence statistics

Figure 3 shows the turbulence statistics measured by PIV at $P1$ on the smooth wall for $U_\infty = 5.95$ and 19.74 m/s and the local Reynolds number $Re_\theta = 1200$ and 3100. The DNS results by Schlatter and Örlü (2010) at $Re_\theta = 1410$ and 3630 are shown as reference for the mean velocity and turbulence statistics profiles. In Fig. 3a, the streamwise velocity profiles in general correspond well with the DNS data despite a small difference ($< 5\%$) between the Reynolds numbers. Near the wall at $y^+ < 10$, the PIV measurement fails to obtain reliable particle displacements due to the light saturation at the wall and the strong velocity gradient in the interrogation window. Similarly, the streamwise velocity fluctuations u'^+_{rms}, the wall-normal velocity fluctuations v'^+_{rms}, and the Reynolds shear stress $\overline{u'v'}^+$ in Fig. 3b show very good agreement with the DNS results except for $y^+ < 10$ where u'^+_{rms} and v'^+_{rms} are slightly biased toward larger values. Furthermore, u'^+_{rms}, v'^+_{rms}, and $\overline{u'v'}^+$ appear to be suppressed at $10 < y^+ < 70$ due to the very fine flow structures that are averaged in the finite interrogation window in the PIV post-processing (Atkinson et al. 2014). At $Re_\theta = 3100$, a more significant attenuation of the velocity fluctuations and Reynolds shear stress is observed

Fig. 3 Wall-normal distributions of the inflow statistics at P_1, $x_1 = 1020\ mm$. **a** mean streamwise velocity at $U_\infty = 5.95\ m/s$ and $Re_\theta = 1200$, **b** Reynolds shear stress and velocity fluctuations in the streamwise and wall-normal direction at $U_\infty = 5.95\ m/s$ and $Re_\theta = 1200$, **c** mean streamwise velocity at $U_\infty = 19.74\ m/s$ and $Re_\theta = 3100$, (d) Reynolds shear stress and velocity fluctuations in the streamwise and wall-normal direction at $U_\infty = 19.74\ m/s$ and $Re_\theta = 3100$. The experimental data are compared with the DNS results from Schlatter and Örlü (2010) at comparable Reynolds number ranges
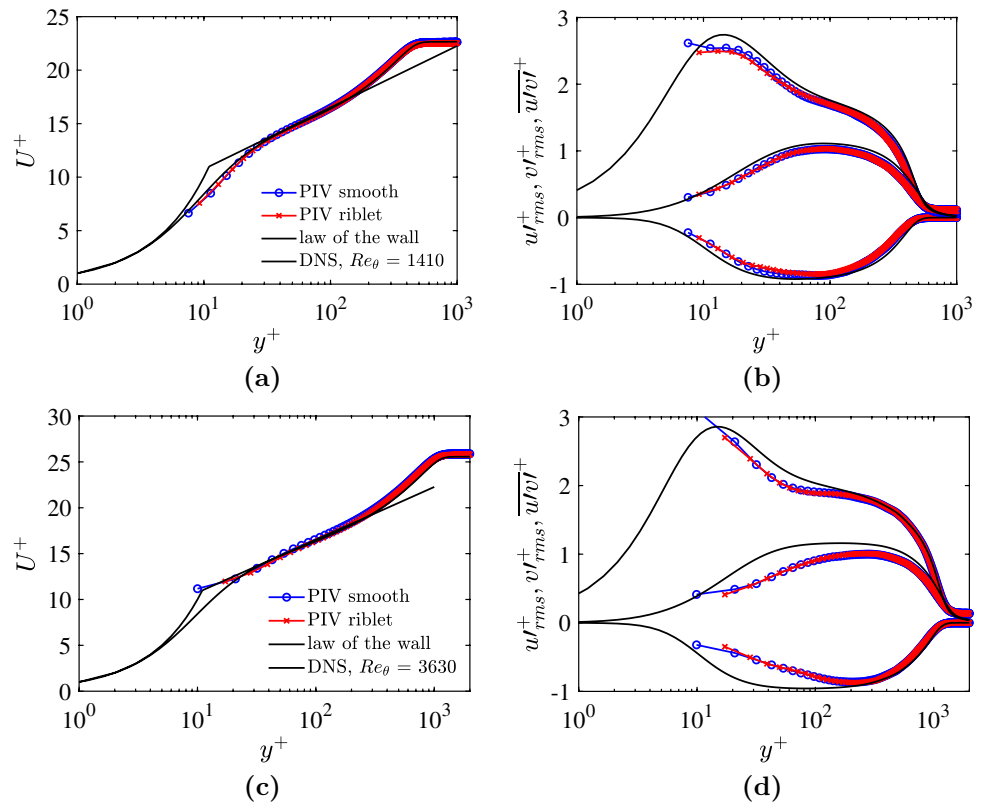
compared to the DNS data due to the stronger velocity gradient and even finer turbulent structures.

The experimental results indicate that the multi-camera PIV system is capable of capturing a large field of view with a reasonable spatial resolution and good measurement accuracy. Although the averaging of the small-scale structures over the interrogation window causes a low-pass filtering effect, the observed discrepancies will not influence the conclusions drawn from the comparison of the large-scale structures between the smooth and riblet surfaces in the following sections.

In Fig. 4, the turbulence statistics measured by PIV and HWA at P_2, i.e., 25 mm upstream of the trailing edge of the riblet insert, are presented for $Re_\theta = 1200$ and 3100 as a function of wall-normal distance in inner scaling for the DR and DI cases. Note that, to compare with the smooth cases and for a consistent definition of the origin, the origin of the wall-normal coordinate for the riblet cases is defined according to the wall-normal offset of $\Delta y = 0.8h$ above the riblet trough. The streamwise velocity distribution is normalized based on the friction velocity of each surface. It is clearly shown that the hotwire results match well with the PIV data. The streamwise velocity profile above the riblet surface depicts an upward shift in the logarithmic region due to a smaller friction velocity for the DR case. The upward shift of the streamwise velocity profile is a result of the energy balance between the reduced kinetic energy

production and viscous dissipation (Choi 1989). For the DI case in Fig. 4 c, a significant downward departure from the smooth behavior in the streamwise velocity distribution indicates the longitudinal grooves to increase the friction drag, i.e., the boundary-layer flow above the too wide riblets is in the drag increase regime.

The distributions of the velocity fluctuations and Reynolds shear stresses along the wall-normal direction above the smooth and riblet surfaces are shown in Fig. 4b and d for the DR and DI cases. A distinct decrease in the streamwise velocity fluctuations u'^+_{rms} is clearly shown in the range of $y^+ < 150$ in Fig. 4b. The weakened streamwise velocity fluctuations are due to the breakup of streamwise vortices by the riblets. For both PIV and HWA results, the maximum intensity of the streamwise velocity fluctuations u'^+_{rms}, that appears around $y^+ \approx 15$, is suppressed by 10 percent indicating a reduced streamwise momentum transfer of the turbulent boundary layer in the near-wall region. Furthermore, in the region of $y^+ < 150$, the wall-normal velocity fluctuations v'^+_{rms} and the Reynolds shear stress $\overline{u'v'}^+$ are lowered. This suggests that the intensity of the turbulent bursting events, i.e., the ejections and sweeps, is significantly weakened, and thus, the energy transport from the outer high-speed flows to the near-wall low-speed flows is decreased. For the DI case in Fig. 4d, an attenuation of the streamwise velocity fluctuations is also observed in the region $y^+ < 80 \sim 100$, whereas for $y^+ > 100$, the streamwise velocity fluctuations are enhanced as previously reported

Fig. 4 Wall-normal distributions of the turbulent statistics at P_2, $x_2 = 1400$ above the smooth and the riblet surfaces. **a** mean streamwise velocity with $U_\infty = 5.95$ m/s and $s^+ = 17$, **b** Reynolds shear stress and velocity fluctuations in the streamwise and wall-normal direction with $U_\infty = 5.95$ m/s and $s^+ = 17$, **c** mean streamwise velocity at $U_\infty = 19.74$ m/s and $s^+ = 50.4$, **d** Reynolds shear stress and velocity fluctuations in the streamwise and wall-normal direction with $U_\infty = 19.74$ m/s and $s^+ = 50.4$. The markers show only one out of every five data points
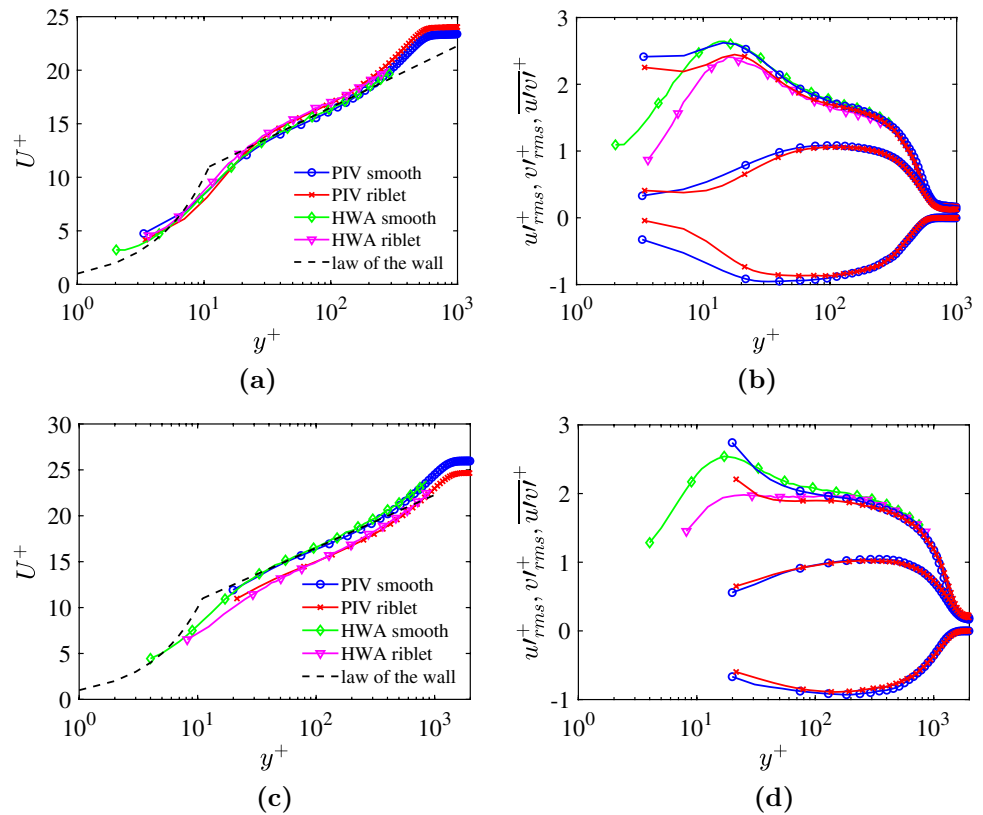
in the turbulent boundary layers above rough walls (Schultz and Flack 2007). This observation indicates that the riblets with too large an extent in the spanwise direction reduce the turbulent intensity in the near-wall region but increase the energy transport in the outer region such that the extra Reynolds shear stress is generated. Unlike turbulent boundary layers above arbitrary rough walls where the total drag is dominated by the form drag, in this study, no pressure drag is generated by riblets and the viscous drag dominates the total drag.

3.3 Structural behavior

3.3.1 Two-point correlation

To analyze the length scales of the turbulent structure, the spatial two-point correlations of the streamwise velocity fluctuations, i.e.,

$$Ruu = \frac{\overline{u'(\vec{x}, t)u'(\vec{x} + \vec{r}, t)}}{\sqrt{\overline{u'^2(\vec{x}, t)}}\sqrt{\overline{u'^2(\vec{x} + \vec{r}, t)}}}, \tag{3}$$

are analyzed. The quantity $\vec{x}$ is the reference point and $\vec{r}$ is the in-plane distance from $\vec{x}$. Figure 5 shows the contours of Ruu above the smooth and riblet surfaces with the reference point located at P_2 of $x_{ref} = 1400$ mm and a wall-normal distance of $y_{ref} = 0.88$ mm, i.e., roughly three times the

riblet height. The wall-normal distance of the reference point in inner coordinates is at $y_{ref}^+ \approx 14.9, 27.5, 44.4$ for the three freestream velocities. The friction velocity $u_{\tau,0}$ over the smooth wall at $P2$ is used for the inner scaling.

In Figure 5 a–f, the distributions of Ruu show similar contour shapes indicating that the global organization of the turbulent structures is qualitatively similar. For the DR case in Fig. 5 (b), the Ruu contour above the riblet surface extends over a longer streamwise distance than the Ruu contour of the smooth surface suggesting that the turbulent structures is elongated in the near-wall region. The illustration in Fig. 6a shows a significant quantitative increase in Ruu in the streamwise direction for the DR case, which agrees with the results reported by Hou et al. (2017) that Ruu decays slower for the drag reducing riblet surface. The enhanced characteristic length of the near-wall flow structures suggests that longer high-speed and low-speed streaks exist above the riblet surface. For the DN and DI cases in Fig. 5d and f, Ruu exhibits a smaller streamwise extent. The quantitative illustrations in Fig. 6b and c show Ruu to decrease more rapidly compared to the smooth case implying that the near-wall streaky structures in the streamwise direction become shorter above the riblet surface similar to the turbulent boundary layer above roughness as reported by Wu and Christensen (2010). In addition, the variation in Ruu between the riblet and

Fig. 5 Spatial two-point correlation of the streamwise velocity fluctuations Ruu above the smooth and the riblet surfaces at P_2 for the DR **a**, **b** DN **c**, **d** and DI **e**, **f** cases. On the left **a**, **c**, **e** the contours for the smooth surface and on the right **b**, **d**, **f** the contours for the riblet surface are shown
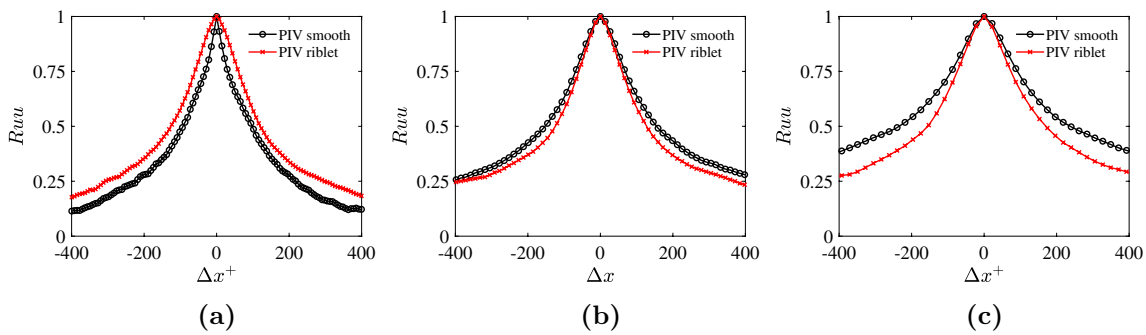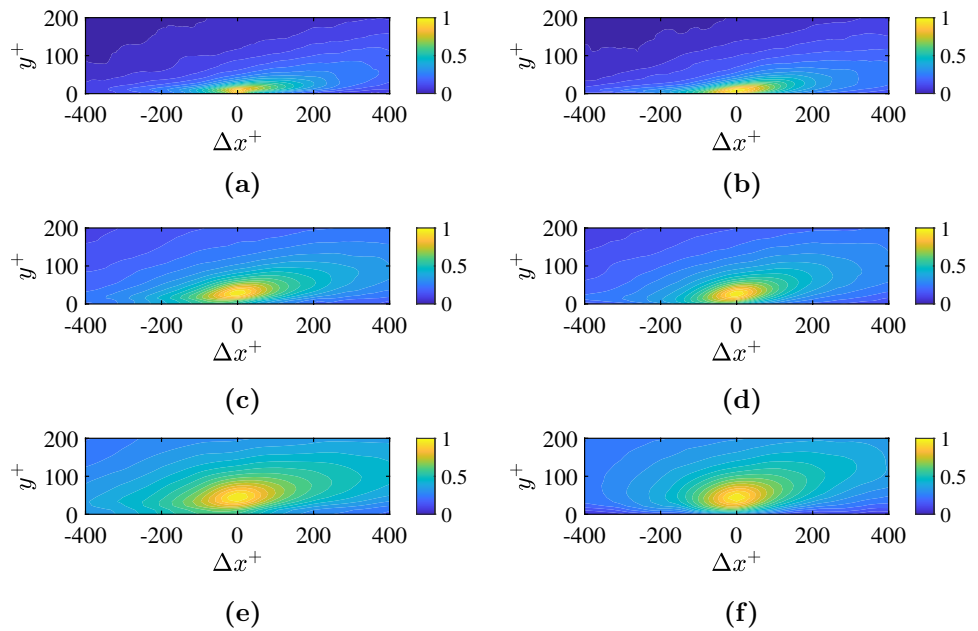
Fig. 6 Comparison of the spatial two-point correlations of the streamwise velocity fluctuations Ruu above the smooth and the riblet surfaces at P_2. **a** DR case, **b** DN case, **c** DI case

smooth wall suggests an direct connection between the drag reduction and the characteristic length scale of the near-wall turbulence above the riblet surface.

3.3.2 Large-scale structures

Figures 7a illustrates an instantaneous distribution of the streamwise velocity u/U_∞ at $U_\infty = 5.97$ m/s above the smooth wall. It is clear that the flow structures are separated by thin layers of strong shear organized into relatively uniform flow regions, i.e., uniform momentum zones (UMZs) (Adrian et al. 2000, de Silva et al. 2016). To analyze the characteristics of the large-scale energetic structures over riblets, the instantaneous UMZs are identified based on the histogram method that has been successfully applied to investigate the organization and dynamics of the large-scale structures in turbulent boundary layers (Adrian et al. 2000,

de Silva et al. 2016, Li et al. 2020). As shown in Fig. 7a, the turbulent/non-turbulent interface (TNTI) illustrated by the solid black line at $y/\delta \approx 0.8$ was identified by a threshold of the local kinetic energy following (Chauhan et al. 2014). Subsequently, the vectors belonging to the turbulent region within a detection window, whose length is denoted by L_x, were used to generate the probability density function (PDF) in Fig. 7b. Each peak in the probability density function (PDF) indicates a UMZ with the local maxima representing the modal velocity U_m of the distinct UMZ.

The mean numbers N_{umz} of UMZs above the smooth and the riblet walls in the DR and DI regimes are shown in Fig. 8a and b as a function of the streamwise extent of the detection window in viscous units, i.e., $L_x^+ = L_x u_\tau / \nu$. To ensure the convergence of the statistics, the flow field above the insert from $x = 1065$ mm to 1425 mm is used to determine the UMZs. For the smooth wall in Fig. 8a,

Fig. 7 Detection of the uniform momentum zones in the turbulent boundary layer. **a** distribution of the freestream velocity u/U_∞, the colored lines indicate the distinct UMZs. **b** probability density function of the streamwise velocity in the detection window with a streamwise extend L_x, $\triangledown$ denotes the modal velocity

(a)

(b)

(a)   (b)   (c)
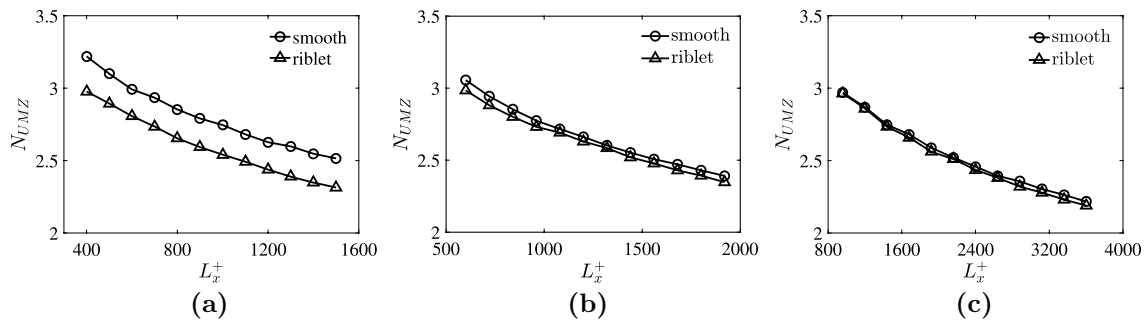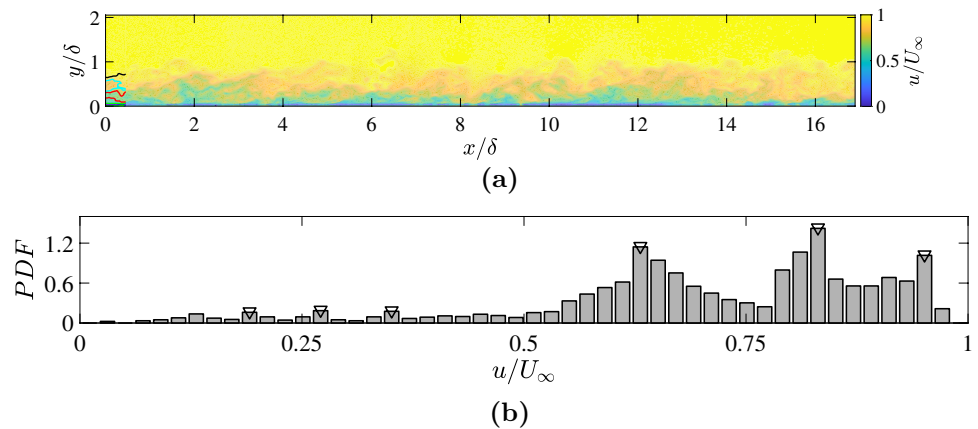
Fig. 8 Comparison of the mean number of uniform momentum zones as a function of the detection window size L_x^+ above the smooth and the riblet surfaces. **a** 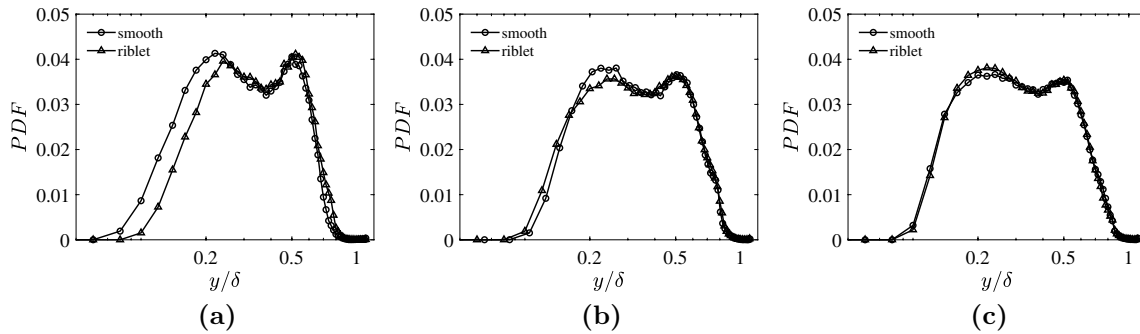DR case at $U_\infty = 5.95$ m/s with $s^+ = 17.0$, **b** DN case at $U_\infty = 11.78$ m/s with $s^+ = 31.7$, **c** DI case at $U_\infty = 19.74$ m/s with $s^+ = 50.4$

N_{umz} decreases from 3.3 to 2.7 when the detection window length L_x^+ varies from 400 to 1500. A similar tendency is also shown for the high Reynolds number flow in Fig. 8 b when L_x^+ varies from 960 to 3600. The results indicate an inconsistency with the observations by de Silva et al. (2016) and Xu et al. (2019) that the dependence on L_x^+ is negligible. In the identification procedure, the detection window acts as an implicit filter on the PDFs of the streamwise velocity (de Silva et al. 2016). It is expected that a large L_x^+ results in a decrease in the mean number of the detected UMZs. The main reason for this inconsistency can be attributed to the PIV spatial resolution and the exclusion of the data below $y^+ < 100$ in de Silva et al. (2016). Despite the disagreement in the effect of the detection window length, the values of N_{umz} at different Reynolds numbers for the smooth wall agree well with the log-linear relation as predicted by de Silva et al. (2016) with comparable L_x^+.

For the DR case with $s^+ = 17.0$, the mean number of UMZ is roughly 10 % lower compared to that of the smooth wall in Fig. 8a. This indicates the population of the strong shear layers that separate the UMZs is reduced, i.e., the coherence of the turbulent structures is enhanced. The current experimental results are in good agreement with

the previous investigations (Guangyao et al. 2019) which showed 8 % lower N_{umz} in a drag reduced turbulent boundary layer. Due to the weakened momentum transfer and turbulent mixing, a lowered N_{umz} can be expected above the riblets. In the DN and DI regime with $s^+ = 31.7$ and 50.4, the mean numbers of the detections remain unchanged for the too large riblets.

To further elucidate the influence of the surface structure on UMZs, the probability density functions (PDFs) of the UMZs are plotted in Fig. 9a, b, and c as a function of the nondimensionalized wall-normal distance y/δ for $s^+ = 17$, 31.7, and 50.4. The PDFs of all cases possess a peak within a wall-normal distance of $y/\delta \approx 0.15 \sim 0.2$, which is attributed to the lowest hairpin packets and the large-scale structures in the logarithmic region. In addition, a plateau of the PDF occurs at $0.3 \le y/\delta \le 0.55$ due to the hairpin packets that develop above the wall Adrian et al. (2000). For the DR case, the UMZs above the riblet surface appear less frequently compared to the smooth wall configuration at $y/\delta \approx 0.05 \sim 0.2$ indicating that the streamwise large-scale structures develop to even larger structures. The distributions of the UMZs are clearly altered at $y^+ < 150$ in Figure 9a in agreement with the

(a)   **(b)**   **(c)**

Fig. 9 Wall-normal distributions of UMZs above the smooth and the riblet surfaces, **a** DR case at $U_\infty = 5.95$ *m/s* with $s^+ = 17.0$, the detection window size $L_x^+ = 1600$, **b** DN case at $U_\infty = 11.78$ m/s with $s^+ = 31.7$, the detection window size $L_x^+ = 1680$, **c** DI case at $U_\infty = 19.74$ m/s with $s^+ = 50.4$, the detection window size $L_x^+ = 1680$

analysis of the streamwise velocity fluctuations. Only the flow structures close to the wall at $y/\delta < 0.3$ respond to the variation in the surface. For the DN and DI case in Fig. 9b, the PDFs show a minor increase in the region of $y/\delta \approx 0.05 \sim 0.3$ due to the oversized riblets. However, despite the small amount of variation in the near-wall region, the mean number of UMZs remains unchanged above the riblets in the drag increase case.

3.3.3 Energy Spectra

Figure 10 shows iso-contours of the pre-multiplied stream-wise energy spectra determined from the hotwire data above the smooth wall and the riblet surface of the DR, DN, and DI cases. The pre-multiplied energy spectra are plotted in the wavelength and wall-normal distance space. Taylor's hypothesis with the local mean velocity as the convection velocity is used to convert the measured frequency spectra into the spatial domain.

(a)   **(b)**   **(c)**

(d)   **(e)**   **(f)**
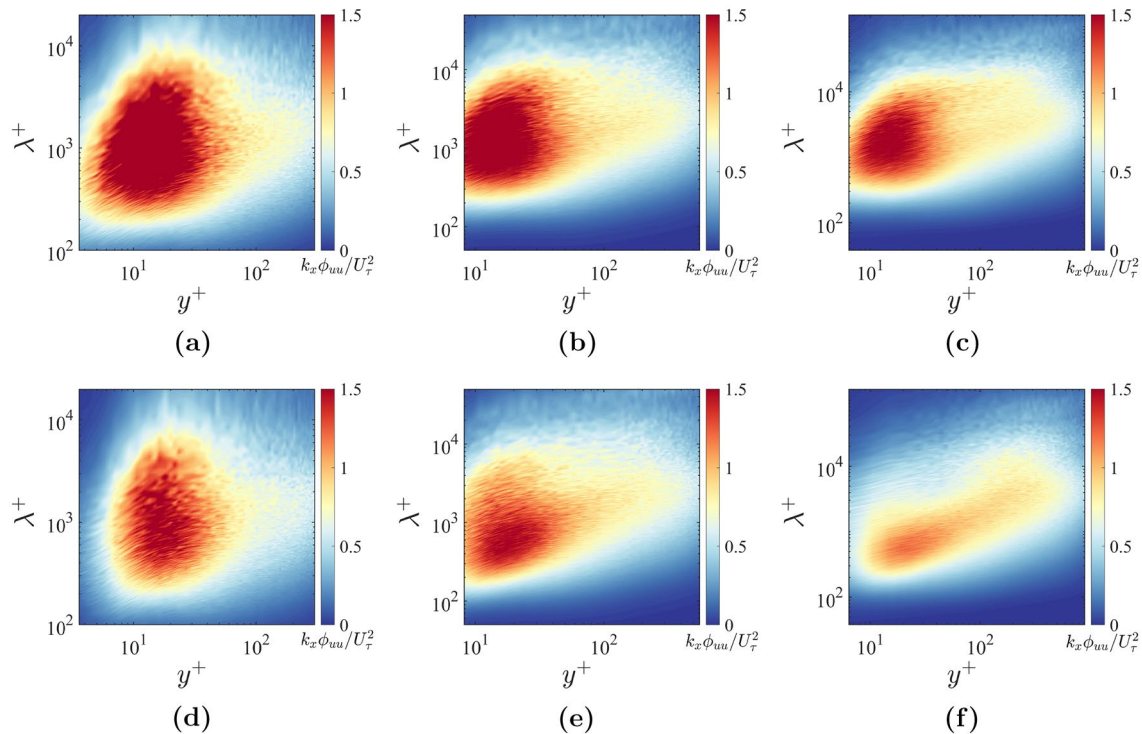
Fig. 10 Pre-multiplied streamwise energy spectra above the smooth and the riblet walls. **a**, **c**, and **d** are for the smooth wall at $U_\infty = 5.95$, 11.78, and 19.74 m/*s*. **b**, **d**, **f** are for the riblet wall at $U_\infty = 5.95$, 11.78, and 19.74 m/*s* corresponding to the DR case with $s^+ = 17.0$, DN case with $s^+ = 31.7$, and DI case with $s^+ = 50.4$

For the lower Reynolds number flows, the energy spectra show similar shapes between the smooth and riblet cases in Fig. 10a and b. The pre-multiplied energy spectrum $k_\lambda \phi_{uu}/u_\tau^2$ peaks at $y^+ \approx 15$ with a wavelength of $\lambda^+ \approx 1000$ for both configurations. Furthermore, a noticeable reduction which is roughly 20% of the peak intensity is observed above the riblet surface. In accordance with the earlier observations (Endrikat et al. 2020, Zi-Liang 2019), the results indicate that the bulk of the kinetic energy is distributed in the range of the wavelength of $\lambda^+ \approx 1000$. The energy peaks at $y^+ \approx 15$ for both cases are associated with the streaky structures and the quasi-streamwise vortices (QSVs) near the wall Schoppa and Hussain (2002). Thus, the suppression of the energy spectra at $y^+ = 15$ evidences that the near-wall flow structures, i.e., the low and high-speed streaks and QSVs are less active above riblets. This is consistent with the previous observations that the drag reduction effect of riblets is associated with the modification of the turbulence production process, i.e., the near-wall turbulence regeneration circle (Karniadakis and Choi 2003, Mamori et al. 2019, Tardu 1995). In Fig. 10 c, a secondary peak emerges for the pre-multiplied energy spectra at $y^+ \approx 100$ roughly with $10^3 \leq \lambda^+ \leq 10^4$ over the smooth surface at a local Reynolds number $Re_\theta = 4363$. This energy peak is associated with the large and very large-scale turbulent structures that populate the logarithmic region Saxton-Fox and McKeon (2017). Above the riblet surface, a significant attenuation of the pre-multiplied streamwise energy spectra compared to the smooth wall is also observed in Fig. 10d similar to the observation in the fully developed rough pipe flows (Rosenberg et al. 2013). The pre-multiplied streamwise energy spectra above the drag increasing riblet surface show a smaller intensity in the near-wall region for wavelength $\lambda^+ > 1000$ indicating that the large-scale structures are less energetic compared to the smooth surface. Moreover, the location of the near-wall peak above the riblet surface remains at $y^+ \approx 15$, whereas the streamwise length scale of the most

energetic structure appears to be around $\lambda^+ \approx 600$. Note that, the near-wall peak of $k_\lambda \phi_{uu}/u_\tau^2$ at $y^+ \approx 15$ in Fig. 10c appears to be smaller at the higher Reynolds number due to the spatial filtering effect of the hotwire. Such phenomena have been reported by Rosenberg et al. (2013) in turbulent pipe flows and by Hutchins et al. (2009) in turbulent boundary-layer flows.

To further assess the influence of riblets on the flow structures, the distributions of the streamwise energy spectra at $y^+ \approx 15$ are compared in Fig. 11a, b, and c for the TBLs of the DR, DN, and DI cases. The results show that the energy distributions in the buffer layer possess a local similarity in the spectra for the wavelengths less than $\lambda^+ \approx 300$, which is consistent with the findings reported by Medjnoun et al. (2018) on smooth walls with spanwise heterogeneities. With respect to the DR case, $k_\lambda \phi_{uu}/u_\tau^2$ is suppressed for the wavelength $\lambda^+ > 300$ in Figure 11a. This indicates that the drag reducing riblet surface has a stronger impact on the large-scale than the small-scale structures. For the DN and DI cases in Fig. 11b and c, the energy is enhanced for the small-scale structures with wavelengths $\lambda^+ < 400$, while it is suppressed for the large scales.

Figure 12a, b and c illustrates the variations between the smooth and the riblet spectra, i.e., $\Delta(k_\lambda \phi_{uu}/u_\tau^2) = (k_\lambda \phi_{uu}/u_\tau^2)_{smooth} - k_\lambda \phi_{uu}/u_\tau^2)_{riblet}$ for the DR, DN, and DI cases. In Fig. 12a, positive $\Delta(k_\lambda \phi_{uu}/u_\tau^2)$ at $y^+ < 100$ indicates turbulent kinetic energy near the wall is suppressed due to the riblet surface. Far from the wall at $y^+ > 100$, the energy spectra are barely affected by the riblet surface, which coincides with Townsend's Reynolds number similarity hypothesis (Townsend 1980). For the DN and DI cases, a noticeable negative $\Delta(k_\lambda \phi_{uu}/u_\tau^2)$ at $10 < y^+ < 40$ emerges for $\lambda^+ \approx 100 - 300$ for the drag neutral and increased cases in Fig. 12b and c. This evidences that additional energy accumulates in the wavelength of $\lambda^+ \approx 100 - 300$ above the semi-circular riblets compared to the smooth wall. The location and the wavelength of the
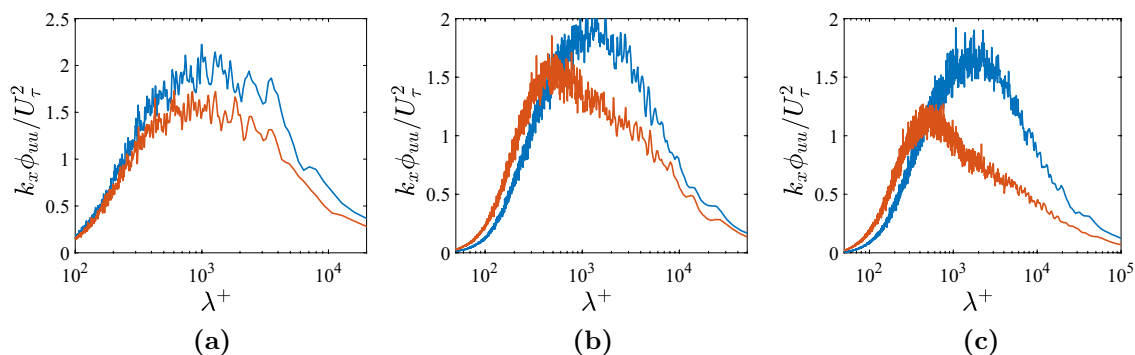
Fig. 11 Pre-multiplied streamwise energy spectra above the smooth and the riblet walls at $y^+ \approx 15$. **a** DR case with $s^+ = 17.0$, **b** DN case with $s^+ = 31.7$, **c** DI case with $s^+ = 50.4$. The blue and red lines indicate the smooth and the riblet cases
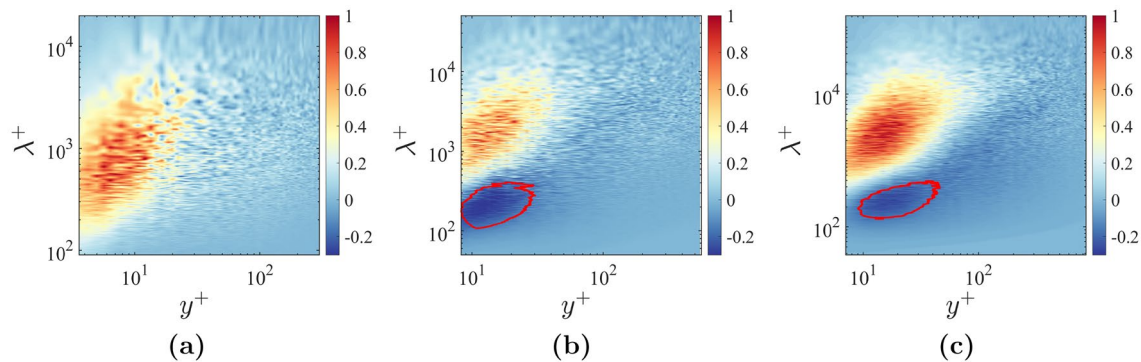
Fig. 12 The variation in the pre-multiplied streamwise energy spectra between the smooth and the riblets walls, i.e., $\Delta(k_\lambda \phi_{uu}/u_\tau^2) = (k_\lambda \phi_{uu}/u_\tau^2)_{smooth} - (k_\lambda \phi_{uu}/u_\tau^2)_{riblet}$. **a** DR case with $s^+ = 17.0$, **b** DN case with $s^+ = 31.7$, **c** DI case with $s^+ = 50.4$. The red lines indicate the contour lines of $\Delta(k_\lambda \phi_{uu}/u_\tau^2) = -0.1$ in **b** and **c**

turbulent structures indicated by the contours in Fig. 12 b and c match those of the spanwise roller-like structures that are reported by Garcia-Mayoral and Jiménez (2011) above oversized blade riblets. Recent numerical studies have shown that for large drag increasing riblets, the spanwise roller-like structures caused by the Kelvin-Helmholtz instability only emerge for certain riblet shapes, i.e., the blade shape or the triangular shape with tip angle of 30° (Endrikat et al. 2021). Indeed, the rolled semi-circular shaped riblets feature a small tip angle of roughly 10 degrees comparable to the blade and triangular shapes that retain sharp tips. With the appearance of the spanwise roller-like structures, the Reynolds shear stress observed in Fig. 4d is enhanced and thus results in the drag reduction breakdown. To the best of our knowledge, experimental evidence of the spanwise roller-like structures above drag increasing riblet surfaces was not reported before.

The experimental results show that the characteristics of the two-point correlations, distributions of UMZs, and pre-multiplied energy spectra are interconnected. In the drag reduction case, the enlarged turbulent characteristic length suggests that the turbulent structures are elongated in the near-wall region. In addition, the intensities of the near-wall large and small-scale turbulent structures are significantly suppressed as indicated by the pre-multiplied energy spectra. These elongated and less energetic near-wall turbulent structures further suppress the formation of the large-scale structures in the downstream and upper region, which is reflected in the population of UMZs. For the wide spaced riblets, the pre-multiplied energy spectra show that the intensity of the large-scale structures are suppressed and small-scale structures with the length scales of $\lambda^+ \approx 100 - 300$ are enhanced immediately above the riblet crest at $10 < y^+ < 40$. The small-scale structures diminish the coherency of the turbulent structures and result in an enhanced viscous dissipation for the DI cases.

4 Summary and conclusion

We conducted PIV and HWA measurements of turbulent boundary-layer flows over semi-circular riblet surfaces to shed light on the variation in the turbulent structures and the underlying mechanisms that result in the degradation of drag reduction. The six-camera 2D-2C PIV system has been employed to measure a large field of view with a favorable spatial resolution such that the structural properties of the turbulent boundary-layer flows in the drag reduction, drag neutral, and drag increase regimes above riblet surface could be investigated. To explore the effect on the structural properties, we examined the development of large-scale structures for drag reduced and drag increased flows. Furthermore, HWA measurements were conducted to determine the streamwise spectrum above the smooth and the riblet surfaces.

The skin friction drag was determined via a modified Clauser method and showed drag variations of -5.75% drag reduction, and 0.3% and 10.7% drag increase for nominal riblet spacings $s^+ = 17$, 31.3, and 50.4. In agreement with previous studies (Choi 1989, Hou et al. 2017), the streamwise velocity profile in inner coordinates shows an upward shift in the logarithmic region due to the reduced kinetic energy production and viscous dissipation for the drag reduction case. Oversized riblets lead to a downward shift of the streamwise velocity indicating a roughness effect. Spatial correlations of the streamwise and wall-normal velocities show an enhanced coherence for the turbulent structures above riblets in the drag reduction regime, i.e., $s^+ = 17$. Moreover, when the riblet size was increased beyond the drag reduction regime, the turbulent structures gradually lose spatial correlation in the streamwise direction. This is an indication of a possible increase in vorticity transport and turbulence production. The large-scale

structures, i.e., UMZs, are less wide spread for the DR case in the logarithmic region than in the smooth case, whereas the wall-normal distributions and the total number of the large-scale structures seem to be hardly affected by the oversized riblets.

The streamwise spectra indicate that the location of the near-wall peak of the streamwise velocity fluctuations above the riblet surface remains at $y^+ \approx 15$ with a wavelength of $\lambda^+ \approx 1000$ for the drag reduction case, whereas the streamwise length scale of the most energetic structure appears to be around $\lambda^+ \approx 600$. Additional energy accumulates at $10 < y^+ < 40$ and $\lambda^+ \approx 100 - 300$ for riblets with $s^+ = 31.3$, and 50.4, which coincide with the spanwise K-H roller structures found by Garcia-Mayoral and Jiménez (2011). These small-scale structures with characteristic wavelength of $\lambda^+ \approx 100 - 300$ lead to an enhanced viscous dissipation for the DI case. Our measurements confirmed that the degradation of drag reduction is related to the K-H roller for the semi-circular riblets. However, it should be noted that the occurrence of the K-H roller depends on geometry and size of the riblet. According to Endrikat et al. (2021), riblets with sharp tips turn to trigger K-H instability, while blunt riblets do not.

Author Contributions W.L. conducted the measurements. W.L., H.X., and W.S. wrote the main manuscript text and S.P. prepared figures 10–12. All authors reviewed the manuscript.

Availability of data and materials The data that support the findings of this study are available from the corresponding author, W.L., upon reasonable request.

Declarations

Conflict of interests The authors declare that they have no conflict of interest.

Ethical Approval Not applicable.

References

Adrian RJ, Meinhart CD, Tomkins CD (2000) Vortex organization in the outer region of the turbulent boundary layer. J Fluid Mech 422:1–54

Atkinson C, Buchmann NA, Amili O, Soria J (2014) On the appropriate filtering of piv measurements of turbulent shear flows. Exp Fluids 55(1):1–15

Bai H, Zhou Y, Zhang W, Xu S, Wang Y, Antonia R (2014) Active control of a turbulent boundary layer based on local surface perturbation. J Fluid Mech 750:316–354

Bechert D, Bartenwerfer M (1989) The viscous flow on surfaces with longitudinal ribs. J Fluid Mech 206:105–129

Bechert DW, Bruse M, Hage W, Van der Hoeven JGT, Hoppe G (1997) Experiments on drag-reduction surfaces and their optimization with an adjustable geometry. J Fluid Mech 338:59–87

Benedict L, Gould R (1996) Towards better uncertainty estimates for turbulence statistics. Exp Fluids 22:129–136

Chauhan K, Philip J, De Silva CM, Hutchins N, Marusic I (2014) The turbulent/non-turbulent interface and entrainment in a boundary layer. J Fluid Mech 742:119–151

Choi K-S (1989) Near-wall wall structure of a turbulent boundary layer with riblets. J Fluid Mech 208:417–458

Chung D, Hutchins N, Schultz MP, Flack KA (2021) Predicting the drag of rough surfaces. Annu Rev Fluid Mech 53:439–471

Daniello RJ, Waterhouse NE, Rothstein JP (2009) Drag reduction in turbulent flows over superhydrophobic surfaces. Phys Fluids 21(8):085103

de Silva CM, Hutchins N, Marusic I (2016) Uniform momentum zones in turbulent boundary layers. J Fluid Mech 786:309–331

Debisschop J, Nieuwstadt F (1996) Turbulent boundary layer in an adverse pressure gradient-effectiveness of riblets. AIAA J 34(5):932–937

Endrikat S, Modesti D, García-Mayoral R, Hutchins N, Chung D (2021) Influence of riblet shapes on the occurrence of kelvin-helmholtz rollers. J Fluid Mech 913:A37

Endrikat S, Modesti D, MacDonald M, García-Mayoral R, Hutchins N, Chung D (2020) Direct numerical simulations of turbulent flow over various riblet shapes in minimal-span channels. Flow, Turbulence and Combustion, pp 1–29

Garcia-Mayoral R, Jiménez J (2011) Drag reduction by riblets Philosophical transactions of the Royal society A: Mathematical, physical and engineering Sciences 369(1940):1412–1427

Garcia-Mayoral R, Jimenez J (2011) Hydrodynamic stability and breakdown of the viscous regime over riblets. J Fluid Mech 678:317–347

Gatti D, Güttler A, Frohnapfel B, Tropea C (2015) Experimental assessment of spanwise-oscillating dielectric electroactive surfaces for turbulent drag reduction in an air channel flow. Exp Fluids 56(5):110

Goldstein D, Tuan T-C (1998) Secondary flow induced by riblets. J Fluid Mech 363:115–151

Gouder K, Potter M, Morrison JF (2013) Turbulent friction drag reduction using electroactive polymer and electromagnetically driven surfaces. Exp Fluids 54:1–12

Guangyao C, Chong P, Di W, Qingqing Y, Jinjun W (2019) Effect of drag reducing riblet surface on coherent structure in turbulent boundary layer. Chin J Aeronaut 32(11):2433–2442

Hirt G, Thome M (2008) Rolling of functional metallic surface structures. CIRP annals 57(1):317–320

Hou J, Hokmabad BV, Ghaemi S (2017) Three-dimensional measurement of turbulent flow over a riblet surface. Exp Therm Fluid Sci 85:229–239

Hutchins N, Nickels TB, Marusic I, Chong M (2009) Hot-wire spatial resolution issues in wall-bounded turbulence. J Fluid Mech 635:103–136

Karniadakis G, Choi K-S (2003) Mechanisms on transverse motions in turbulent wall flows. Annu Rev Fluid Mech 35(1):45–62

Kasagi N, Suzuki Y, Fukagata K (2009) Microelectromechanical Systems-Based Feedback Control of Turbulence for Skin Friction Reduction. Annual Rev Fluid Mech 41:231–251

Lee C, Kim C-J (2011) Underwater restoration and retention of gases on superhydrophobic surfaces for drag reduction. Phys Rev Lett 106(1):014502

Lee S-J, Lee S-H (2001) Flow field analysis of a turbulent boundary layer over a riblet surface. Exp Fluids 30(2):153–166

Li W, Roggenkamp D, Paakkari V, Klaas M, Soria J, Schröder W (2020) Analysis of a drag reduced flat plate turbulent boundary layer via uniform momentum zones. Aerosp Sci Technol 96:105552

Li Z, Hu B, Lan S, Zhang J, Huang J (2015) Control of turbulent channel flow using a plasma-based body force. Comput Fluids 119:26–36

Ligrani P, Bradshaw P (1987) Spatial resolution and measurement of turbulence in the viscous sublayer using subminiature hot-wire probes. Exp Fluids 5(6):407–417

Luchini P, Manzo F, Pozzi A (1991) Resistance of a grooved surface to parallel flow and cross-flow. J Fluid Mech 228:87–109

Mamori H, Yamaguchi K, Sasamori M, Iwamoto K, Murata A (2019) Dual-plane stereoscopic piv measurement of vortical structure in turbulent channel flow on sinusoidal riblet surface. Eur J Mech-B/Fluids 74:99–110

Martin S, Bhushan B (2014) Fluid flow analysis of a shark-inspired microstructure. J Fluid Mech 756:5–29

Medjnoun T, Vanderwel C, Ganapathisubramani B (2018) Characteristics of turbulent boundary layers over smooth surfaces with spanwise heterogeneities. J Fluid Mech 838:516–543

Modesti D, Endrikat S, Hutchins N, Chung D (2021) Dispersive stresses in turbulent flow over riblets. J Fluid Mech 917:A55

Monty J, Dogan E, Hanson R, Scardino A, Ganapathisubramani B, Hutchins N (2016) An assessment of the ship drag penalty arising from light calcareous tubeworm fouling. Biofouling 32(4):451–464

Nugroho B, Hutchins N, Monty JP (2013) Large-scale spanwise periodicity in a turbulent boundary layer induced by highly ordered and directional surface roughness. Inter J Heat Fluid Flow 41:90–102

Perry A, Li JD (1990) Experimental support for the attached-eddy hypothesis in zero-pressure-gradient turbulent boundary layers. J Fluid Mech 218:405–438

Raayai-Ardakani S, McKinley GH (2017) Drag reduction using wrinkled surfaces in high reynolds number laminar boundary layer flows. Phys Fluids 29(9):093605

Rosenberg BJ, Hultmark M, Vallikivi M, Bailey S, Smits AJ (2013) Turbulence spectra in smooth- and rough-wall pipe flow at extreme reynolds numbers. J Fluid Mech 731:46–63

Saxton-Fox T, McKeon BJ (2017) Coherent structures, uniform momentum zones and the streamwise energy spectrum in wall-bounded turbulent flows. J Fluid Mech 826:R6

Schlatter P, Örlü R (2010) Assessment of direct numerical simulation data of turbulent boundary layers. J Fluid Mech 659:116–126

Schoppa W, Hussain F (2002) Coherent structure generation in near-wall turbulence. J Fluid Mech 453:57–108

Schrauf G, Gölling B, Wood N. KATnet - Key Aerodynamic Technologies for Aircraft Performance Improvement. In *5th Community Aeronautical Days*, Wien, Austria, (2006)

Schultz MP, Flack KA (2007) The rough-wall turbulent boundary layer from the hydraulically smooth to the fully rough regime. J Fluid Mech 580:381–405

Soria J (1996) An investigation of the near wake of a circular cylinder using a video-based digital cross-correlation particle image velocimetry technique. Exp Thermal Fluid Sci 12(2):221–233

Spalart PR, McLean JD (2011) Drag reduction: enticing turbulence, and then an industry. Philosophical Transactions of the Royal Society A: Mathematical, Physical and Engineering Sciences 369(1940):1556–1569

Szodruch J. Viscous drag reduction on transport aircraft. *AIAA Paper*, 1991-685, (1991)

Tardu SF (1995) Coherent structures and riblets. Appl Sci Res 54(4):349–385

Tiainen J, Grönman A, Jaatinen-Värri A, Pyy L (2020) Effect of non-ideally manufactured riblets on airfoil and wind turbine performance. Renew Energ 155:79–89

Townsend A. *The structure of turbulent shear flow*. Cambridge university press, (1980)

Walsh M. Turbulent boundary layer drag reduction using riblets. *AIAA Paper*, 1982-169, (1982)

Walsh M (1983) Riblets as a viscous drag reduction technique. AIAA J 21:485–486

Walsh M, Lindemann A. Optimization and application of riblets for turbulent drag reduction. *AIAA Paper*, 1984-347, (1984)

Westerweel J, Scarano F (2005) Universal Outlier Detection for PIV Data. Exp Fluids 39:1096–1100

Wong CW, Cheng X, Fan D, Li W, Zhou Y (2021) Friction drag reduction based on a proportional-derivative control scheme. Phys Fluids 33(7):075115

Wu Y, Christensen KT (2010) Spatial structure of a turbulent boundary layer with irregular surface roughness. J Fluid Mech 655:380–418

Xu F, Zhong S, Zhang S (2019) Statistical analysis of vortical structures in turbulent boundary layer over directional grooved surface pattern with spanwise heterogeneity. Phys Fluids 31(8):085110

Zi-Liang Zhang (2019) Ming-Ming, Zhang, Chang, Cai, Yu, and Cheng. Characteristics of large- and small-scale structures in the turbulent boundary layer over a drag-reducing riblet surface: Proceedings of the Institution of Mechanical Engineers, Part C: Journal of Mechanical Engineering Science 234(3):796–807